Atmos. Chem. Phys., 16, 12287–12303, 2016
www.atmos-chem-phys.net/16/12287/2016/
doi:10.5194/acp-16-12287-2016

Atmospheric Chemistry and Physics Open Access EGU

Investigation of ice particle habits to be used for ice cloud remote sensing for the GCOM-C satellite mission

Husi Letu[1,2], Hiroshi Ishimoto[3], Jerome Riedi[4], Takashi Y. Nakajima[1], Laurent C.-Labonnote[4], Anthony J. Baran[5], Takashi M. Nagao[6], and Miho Sekiguchi[7]

[1]Research and Information Center (TRIC), Tokai University, 4-1-1 Kitakaname Hiratsuka, Kanagawa 259-1292, Japan
[2]Institute of Remote Sensing and Digital Earth, Chinese Academy of Sciences (CAS), DaTun Road No. 20 (North), Beijing 100101, China
[3]Meteorological Research Institute, 1-1 Nagamine, Tsukuba, Ibaraki 305-0052, Japan
[4]Laboratoire d'Optique Atmosphérique, UMR CNRS 8518, Université de Lille 1-Sciences et Technologies, Villeneuve d'Ascq, France
[5]Met Office, Fitzroy Road, Exeter, EX1 3PB, UK
[6]Earth Observation Research Center (EORC), Japan Aerospace Exploration Agency (JAXA), 2-1-1 Sengen Tsukuba, Ibaraki 305-8505, Japan
[7]Tokyo University of Marine Science and Technology, Tokyo 135-8533, Japan

Correspondence to: Takashi Y. Nakajima (nkjm@yoyogi.ycc.u-tokai.ac.jp)

Received: 29 September 2015 – Published in Atmos. Chem. Phys. Discuss.: 11 November 2015
Revised: 10 September 2016 – Accepted: 15 September 2016 – Published: 29 September 2016

Abstract. In this study, various ice particle habits are investigated in conjunction with inferring the optical properties of ice clouds for use in the Global Change Observation Mission-Climate (GCOM-C) satellite programme. We develop a database of the single-scattering properties of five ice habit models: plates, columns, droxtals, bullet rosettes, and Voronoi. The database is based on the specification of the Second Generation Global Imager (SGLI) sensor on board the GCOM-C satellite, which is scheduled to be launched in 2017 by the Japan Aerospace Exploration Agency. A combination of the finite-difference time-domain method, the geometric optics integral equation technique, and the geometric optics method is applied to compute the single-scattering properties of the selected ice particle habits at 36 wavelengths, from the visible to the infrared spectral regions. This covers the SGLI channels for the size parameter, which is defined as a single-particle radius of an equivalent volume sphere, ranging between 6 and 9000 µm. The database includes the extinction efficiency, absorption efficiency, average geometrical cross section, single-scattering albedo, asymmetry factor, size parameter of a volume-equivalent sphere, maximum distance from the centre of mass, particle volume, and six nonzero elements of the scattering phase matrix. The characteristics of calculated extinction efficiency, single-scattering albedo, and asymmetry factor of the five ice particle habits are compared. Furthermore, size-integrated bulk scattering properties for the five ice particle habit models are calculated from the single-scattering database and microphysical data. Using the five ice particle habit models, the optical thickness and spherical albedo of ice clouds are retrieved from the Polarization and Directionality of the Earth's Reflectances-3 (POLDER-3) measurements, recorded on board the Polarization and Anisotropy of Reflectances for Atmospheric Sciences coupled with Observations from a Lidar (PARASOL) satellite. The optimal ice particle habit for retrieving the SGLI ice cloud properties is investigated by adopting the spherical albedo difference (SAD) method. It is found that the SAD is distributed stably due to the scattering angle increases for bullet rosettes with an effective diameter (D_{eff}) of 10 µm and Voronoi particles with D_{eff} values of 10, 60, and 100 µm. It is confirmed that the SAD of small bullet-rosette particles and all sizes of Voronoi particles has a low angular dependence, indicating that a combination of the bullet-rosette and Voronoi models is sufficient for retrieval of the ice cloud's spherical albedo and optical thickness as effective habit models for the SGLI

sensor. Finally, SAD analysis based on the Voronoi habit model with moderate particle size ($D_{\text{eff}} = 60\,\mu\text{m}$) is compared with the conventional general habit mixture model, inhomogeneous hexagonal monocrystal model, five-plate aggregate model, and ensemble ice particle model. The Voronoi habit model is found to have an effect similar to that found in some conventional models for the retrieval of ice cloud properties from space-borne radiometric observations.

1 Introduction

Ice clouds play an important role in the radiation balance of the Earth's atmospheric system through interaction with solar radiation and infrared emissions (Liou, 1986). However, large uncertainties exist in quantifying the radiative impact of ice clouds. This is because they consist of ice particles with various microphysical characteristics, e.g. a wide range of habits and sizes (C.-Labonnote et al., 2000; Forster et al., 2007; Baran et al., 2007; Cole et al., 2014; Yang et al., 2015). Different ice particle habits have varying single-scattering characteristics, resulting in different radiative properties. Satellite observations are important as a means of inferring the ice clouds' optical properties and monitoring their radiative impact on a global climate system. However, retrieved ice cloud properties highly depend on the assumed ice particle model. In practice, one chooses an ice particle model, which may consist of a single habit or a mixture of habits, and look-up tables (LUTs) for ice cloud reflection and transmission characteristics are computed for a range of input optical properties such as optical thickness, cloud temperature, and effective particle size. The LUTs and a fast radiative transfer model are subsequently used for global operational retrievals. Thus, the choice of an ice particle model for a given satellite mission deserves rigorous investigation. The present study aims to better understand the performance of several ice cloud habit models, in conjunction with applications to the Global Change Observation Mission-Climate (GCOM-C) satellite mission.

Over the past 2 decades, aircraft and balloon in situ observations have contributed greatly to understanding ice cloud microphysical characteristics and radiative properties (Baran et al., 1998, 1999, 2003; Heymsfield et al., 2002; Heymsfield, 2003; Zhang et al., 2009). A variety of ice particle models has been developed based on in situ observations of ice particle habits and their single-scattering properties (e.g. Macke et al., 1996a, b; McFarquhar and Heymsfield, 1996; Yang et al., 2000, 2005, 2013; Um and McFarquhar, 2007, 2009, 2011; Nousiainen et al., 2011; Baum et al., 2005, 2011; Baran and C.-Labonnote, 2007; Ishimoto et al., 2012b; Liu et al., 2014a). Numerous light-scattering computation methods have been employed to calculate the single-scattering properties of the various ice particles, including the finite-difference time-domain (FDTD) method (Yee, 1966; Yang and Liou, 1998a; Sun et al., 1999, Ishimoto et al., 2012a), the T-matrix (Baran et al., 2001; Bi and Yang, 2014a, b), the discrete dipole approximation method (Purcell and Pennypacker, 1973; Draine and Flatau, 1994; Yurkin et al., 2007), the boundary element method (Mano, 2000; Groth et al., 2015), the pseudo-spectral time-domain method (Liu, 1997, 1998; Chen et al., 2008; Liu et al., 2012), the surface-integral equation method (Nakajima et al., 2009), the improved geometric optics method (IGOM) (Yang and Liou, 1996), geometric optics integral equation (GOIE) (Yang and Liou, 1996; Ishimoto et al., 2012a), and the ray-tracing geometric optics method (GOM) (Takano and Liou, 1989, 1993; Macke, 1993; Macke et al., 1996a; Yang and Liou, 1998b; Masuda et al., 2012).

Various ice particle models correspond to different radiative properties. Quantifying optical properties of these ice particle models is computationally expensive, and thus for application purposes it is useful to establish a number of libraries that pre-calculate the single-scattering properties of various ice particle habits. Using hexagonal plates and columns with a random orientation, Hess and Wiegner (1994) developed a single-scattering property database at wavelengths between 0.35 and 3.7 µm. Additionally, Yang et al. (2000) provided a database at wavelengths between 0.2 and 5 µm for six ice particle habits (plates, solid and hollow columns, planar bullet rosettes, spatial bullet rosettes, and aggregates); Yang et al. (2005) further included two more ice habits and extended the database to wavelengths between 3 and 100 µm. Recently, Yang et al. (2013) released a database of a full set of scattering, absorption, and polarisation properties, assuming random orientation for a set of 11 habits at a number of wavelengths, ranging between 0.2 and 100 µm. This database involved the addition of roughness to the particle surfaces. This library is based on the Amsterdam discrete dipole approximation, T-matrix, and IGOM methods. Using this updated library, Baum et al. (2014) developed a new set of bulk scattering and absorption models, with habit mixtures for radiative transfer calculations and remote sensing retrievals of ice clouds.

There is increasing evidence that the ice particle model should contain some degree of surface roughness (Foot, 1988; Baran et al., 2001, 2003; Ottaviani et al., 2012; van Diedenhoven et al., 2012, 2013, 2014; Cole et al., 2013, 2014; Holz et al., 2016). In particular, using an ensemble ice particle model, Baran and C.-Labonnote (2007) and Baran et al. (2014) showed that featureless phase functions best fitted their multi-angle satellite measurements at solar wavelengths. Interestingly, using particle images of convective ice clouds from in situ measurements, Ishimoto et al. (2012b) developed a new habit of complex and highly irregular shapes, called the Voronoi aggregate. The phase function of the Voronoi habit varies smoothly with the scattering angle, which is similar to behaviour found from assuming severe surface roughness, including bubbles within the particle, or a combination of included bubbles and surface roughness.

However, use of the Voronoi habit model for retrieval of the ice cloud's optical thickness has not yet been investigated.

Numerous articles have investigated the use of optimal ice particle habits derived from various ice habit models and remote sensing measurements from multiple angles, for use in cloud parameter retrievals (Baran et al., 1998, 1999, 2003, 2007; Chepfer et al., 1998; C.-Labonnote et al., 2000; Chepfer et al., 2001; Masuda et al., 2002; Knap et al., 2005; Sun et al., 2006; Baran and C.-Labonnote, 2006). C.-Labonnote et al. (2000, 2001) and Doutriaux-Boucher et al. (2000) developed models of randomly oriented hexagonal ice particles containing spherical air bubbles (the inhomogeneous hexagonal monocrystal (IHM) model) for use in the ice cloud retrievals of the POLarization and Directionality of the Earth's Reflectances (POLDER) measurements. Spherical albedo difference (SAD) analysis is employed to investigate the capability of the IHM model for retrieving the optical properties of ice clouds. It is illustrated that POLDER multi-angle measurements are sensitive to ice particle habits and roughness, at least for ice clouds having an optical thickness larger than 5. Chepfer et al. (2002) investigated effective ice particle habits using multi-angle and multi-satellite methods derived from visible reflectance satellite measurements.

The Second Generation Global Imager (SGLI) on board the GCOM-C satellite, scheduled for launch in 2017 by the Japan Aerospace Exploration Agency (JAXA), measures radiation at 19 visible and near-infrared wavelengths in order to understand the global radiation budget, carbon cycle mechanism, and climate change (Imaoka et al., 2010). Since retrieving ice cloud properties on a global scale from satellite observations requires knowledge of ice microphysical models, it is crucial to identify an optimal choice of ice habits for SGLI. The objectives of this study are to better understand the performance of existing ice models used in other satellite missions, investigate the potential of the Voronoi model, and provide a recommendation for the GCOM-C.

The paper is organised as follows. In Sect. 2, in order to develop the ice cloud property products of the GCOM-C satellite, we describe the method for calculating single-scattering properties at the SGLI-operated wavelengths for the five ice particle habits, including the Voronoi model. In Sect. 3, we apply the newly calculated ice cloud properties to SAD analysis, using POLDER measurements as an example. In Sect. 4, we describe the results of the SAD analysis. Section 5 presents our conclusions.

2 Ice cloud models for the SGLI sensor

2.1 Single-scattering properties

Single-scattering properties for the five ice particle habits are calculated for the SGLI observation channels. The single-scattering properties are used to determine the optimal ice particle habits, using the SAD method. The SGLI is the successor sensor to the Global Imager (GLI) aboard ADEOS-II, which takes measurements at wavelengths ranging from the near-ultraviolet to the thermal infrared. The first satellite, GCOM-C1, is scheduled for launch in 2017 by the JAXA. The GCOM-C mission intends to establish a long-term satellite-observation system to measure essential geophysical parameters on the Earth's surface and in the atmosphere on a global scale to facilitate the understanding of the global radiation budget, carbon cycle mechanism, and climate change (Imaoka et al., 2010). As shown in Table 1, SGLI has 19 channels, including two polarisation channels at visible and near-infrared wavelengths. A detailed description of the SGLI is reported by Imaoka et al. (2010), Nakajima et al. (2011), and Letu et al. (2012).

Table 1. Specification of the SGLI.

No.	SGLI channels	Center wavelength (μm)	Band width (nm)	IFOV (m)
1	VN1	0.380	10	250
2	VN2	0.412	10	250
3	NV3	0.443	10	250
4	NV4	0.490	10	250
5	NV5	0.530	20	250
6	NV6	0.565	20	250
7	NV7	0.673	20	250
8	NV8	0.673	20	250
9	NV9	0.763	12	1000
10	NV10	0.868	20	250
11	NV11	0.868	20	250
12	P1	0.673	20	1000
13	P2	0.868	20	1000
14	SW1	1.050	20	1000
15	SW2	1.380	20	1000
16	SW3	1.630	200	250
17	SW4	2.210	50	1000
18	T1	10.8	740	500
19	T2	12.0	740	500

Four of the ice particle habits (hexagonal columns, plates, bullet rosettes, and droxtals) employed in this study were chosen by referring to the MODIS Collection 5 ice particle model (Baum et al., 2005) and ice cloud in situ measurement data. The habits shown in Fig. 1 are defined with the same parameters (semi-width, length, aspect ratio, and maximum dimension) as were employed in the scattering properties database by Yang et al. (2000, 2005). The Voronoi habit was numerically determined by extraction of Wigner–Seitz cells from a 3-D mosaic image of the ice cloud microphysical data (Ishimoto et al., 2012b). This habit is different from the aggregate model used in the scattering database reported by Yang and Liou (1998b) and Yang et al. (2013). Spatial Poisson–Voronoi tessellations were used to determine the complex structure of the ice particles for the 3-D mosaic image. The geometry of each cell in the Voronoi tessellation

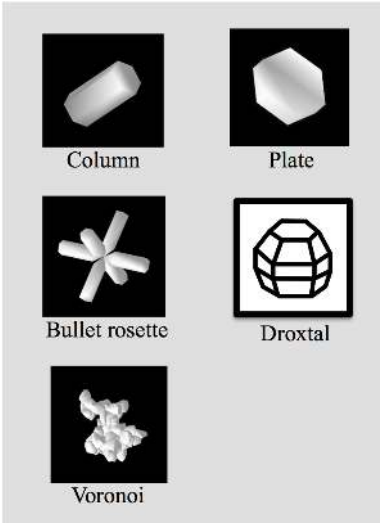

Figure 1. SGLI cloud particle habits.

was defined and based on the method by Ohser and Mücklich (2000).

A combination of the FDTD, GOIE, and GOM methods was employed to calculate the single-scattering properties of Voronoi ice habits for a wide range of size parameters (SZP) and is given by

$$\mathrm{SZP} = 2\pi \cdot re/\lambda. \quad (1)$$

The refractive index of ice, published by Warren and Brandt (2008), is used in the computations. As shown in Table 2, the FDTD method is used to calculate the single-scattering properties of ice particles with small size parameters (SZP < 50). The GOIE and GOM methods are employed for calculating the scattering properties of ice particles with medium and large parameters, respectively. The wavelength selected for detailed calculations is determined by optimising the results of the scattering database for the SGLI channels (Letu et al., 2012). Calculations are performed at 27 spectral wavelengths (λ) from the visible to the infrared spectral region in the SGLI channels shown in Table 2. The volume-equivalent radius (re) ranges from 0.7 to 533 µm and is defined as a single-particle radius of an equivalent volume sphere. The SZP ranges from 0.35 to 6098.

Consideration of the edge effect (Bi et al., 2010; Bi and Yang, 2014a) is important for calculating the extinction efficiency (Q_{ext}) and absorption efficiency (Q_{abs}) by the GOIE method when the size parameter is less than 1000. The treatment of the edge effect is based on the method proposed by Bi et al. (2011) and Ishimoto et al. (2012a). Correction coefficients are calculated from comparison results of the FDTD and GOIE as

$$Q_{\mathrm{ext}} = Q_{\mathrm{ext/GOIE}} + K_1 \cdot \mathrm{SZP}^{2/3},$$
$$Q_{\mathrm{abs}} = Q_{\mathrm{abs/GOIE}} + K_2 \cdot \mathrm{SZP}^{2/3}, \quad (2)$$

where $Q_{\mathrm{ext/GOIE}}$ and $Q_{\mathrm{abs/GOIE}}$ are the extinction efficiencies calculated by the GOIE method. K_1 and K_2 are the coefficients of the edge-effect contribution. These coefficients are applied to correct the Q_{ext} and Q_{abs} of large particles calculated using GOIE; they are calculated by comparing Q_{ext} and Q_{abs} obtained from FDTD and GOIE for maximum extension from the centre of mass, ranging from 30 to 60 µm.

2.2 Microphysical data and bulk scattering properties of the ice particle model

In this study, microphysical data obtained during 11 field campaigns were used to generate the particle size distributions (PSDs) of ice crystals using Eq. (3). To ensure the PSDs are unambiguously those of ice, microphysical data were filtered by limiting the cloud temperature to $T \leq -40\,^{\circ}\mathrm{C}$. More than 14 000 individual PSDs were selected to build bulk scattering properties of the ice particle models (Heymsfield et al., 2013). The microphysical data were obtained from the Space Science and Engineering Center, University of Wisconsin-Madison (http://www.ssec.wisc.edu/ice_models/microphysical_data.html), and the PSDs are described by the following equation:

$$n(D) = N_0 D^{\mu} e^{-\lambda D}, \quad (3)$$

where D is the particle maximum dimension, $n(D)$ is the particle concentration per unit volume, N_0 is the intercept, λ is the slope, and μ is the dispersion.

Furthermore, spectral bulk scattering properties were calculated from SGLI single-scattering database, and the derived PSDs were based on the method described in Baum et al. (2011). The main steps for calculating the bulk scattering properties are as follows:

1. Extract the total projected area, total volume, maximum dimension, scattering cross section, and scattering phase function parameters at a specific wavelength for five ice particle models from the SGLI single-scattering property database.

2. Calculate the effective diameter (D_{eff}) for 5 ice particle models based on Eq. (4).

3. Calculate the bulk-averaged single-scattering albedo ($\overline{A_{\mathrm{s}}}$), asymmetry factor ($\overline{g}$), extinction efficiency ($\overline{Q_{\mathrm{e}}}$) and scattering phase function ($\overline{P}$) for five ice particle models based on Eqs. (5)–(8).

4. Select the single-scattering albedo, asymmetry factor, extinction efficiency, and scattering phase function with small, medium, and large D_{eff}s, and average the selected

Table 2. Size parameter with various particle size and calculating wavelength on the SGLI channels (FDTD, GOIE, GOM).

$\widetilde{r}$(μm) λ (μm)	0.5500	0.5650	0.5800	0.6590	0.6740	0.6860	0.8530	0.8650	0.8830
0.700	7.997	7.784	7.583	6.674	6.526	6.411	5.156	5.085	4.981
1.000	11.424	11.121	10.833	9.534	9.322	9.159	7.366	7.264	7.116
1.300	14.851	14.457	14.083	12.395	12.119	11.907	9.576	9.443	9.250
1.900	21.706	21.129	20.583	18.115	17.712	17.402	13.995	13.801	13.520
2.600	29.702	28.914	28.166	24.790	24.238	23.814	19.152	18.886	18.501
3.500	39.984	38.922	37.916	33.370	32.628	32.057	25.781	25.423	24.905
4.900	55.977	54.491	53.082	46.719	45.679	44.880	36.093	35.593	34.867
6.900	78.825	76.733	74.748	65.788	64.323	63.198	50.825	50.120	49.099
9.500	108.528	105.646	102.914	90.577	88.561	87.012	69.977	69.006	67.599
13.200	150.796	146.793	142.997	125.854	123.053	120.901	97.231	95.882	93.928
18.200	207.916	202.396	197.162	173.527	169.665	166.697	134.061	132.201	129.506
25.300	289.027	281.353	274.077	241.221	235.853	231.727	186.359	183.774	180.028
35.100	400.981	390.336	380.241	334.658	327.210	321.487	258.546	254.959	249.762
47.300	540.354	5307.901	5170.628	4550.780	4449.502	4371.668	3515.785	3467.011	3396.336
60.600	692.293	673.913	656.485	577.786	564.927	555.045	446.379	440.186	431.213
77.100	880.788	857.405	835.230	735.104	718.744	706.171	567.917	560.039	548.622
97.500	1113.837	1084.266	1056.225	929.606	908.918	893.018	718.184	708.220	693.783
122.800	1402.864	1365.620	1330.302	1170.827	1144.770	1124.745	904.543	891.994	873.811
154.000	1759.292	1712.585	1668.294	1468.301	1435.624	1410.511	1134.362	1118.625	1095.822
192.700	2201.400	2142.955	2087.534	1837.283	1796.394	1764.971	1419.425	1399.734	1371.200
242.300	2768.029	2694.541	2624.855	2310.191	2258.777	2219.265	1784.778	1760.018	1724.140
308.400	3523.153	3429.618	3340.921	2940.416	2874.977	2824.686	2271.670	2240.155	2194.490
416.380	4756.714	4630.430	4510.677	3969.943	3881.592	3813.692	3067.049	3024.500	2962.846
533.800	6098.117	5936.220	5782.697	5089.475	4976.208	4889.161	3931.963	3877.415	3798.374
	1.0350	1.0500	1.0650	1.3650	1.3800	1.3950	1.4800	1.6300	1.7800
0.700	4.249	4.189	4.130	3.222	3.187	3.153	2.972	2.698	2.471
1.000	6.071	5.984	5.900	4.603	4.553	4.504	4.245	3.855	3.530
1.300	7.892	7.779	7.670	5.984	5.919	5.855	5.519	5.011	4.589
1.900	11.534	11.370	11.209	8.746	8.651	8.558	8.066	7.324	6.707
2.600	15.784	15.558	15.339	11.968	11.838	11.711	11.038	10.022	9.178
3.500	21.247	20.944	20.649	16.111	15.936	15.764	14.859	13.492	12.355
4.900	29.746	29.322	28.909	22.555	22.310	22.070	20.802	18.888	17.296
6.900	41.888	41.290	40.708	31.761	31.416	31.078	29.293	26.598	24.356
9.500	57.672	56.848	56.047	43.729	43.254	42.789	40.331	36.620	33.534
13.200	80.133	78.989	77.876	60.760	60.100	59.454	56.039	50.882	46.594
18.200	110.487	108.909	107.375	83.776	82.865	81.974	77.266	70.156	64.244
25.300	153.589	151.395	149.263	116.458	115.192	113.953	107.409	97.524	89.306
35.100	213.082	210.038	207.080	161.568	159.811	158.093	149.013	135.300	123.899
47.300	2897.550	2856.157	2815.929	2197.043	2173.163	2149.795	2026.327	1839.855	1684.811
60.600	367.885	362.630	357.522	278.946	275.914	272.947	257.271	233.596	213.911
77.100	468.052	461.365	454.867	354.896	351.039	347.264	327.320	297.199	272.154
97.500	591.894	583.439	575.221	448.799	443.921	439.147	413.926	375.835	344.163
122.800	745.483	734.833	724.484	565.257	559.112	553.100	521.335	473.359	433.469
154.000	934.889	921.534	908.554	708.872	701.167	693.628	653.791	593.626	543.601
192.700	1169.826	1153.114	1136.873	887.011	877.369	867.935	818.088	742.804	680.208
242.300	1470.933	1449.920	1429.498	1115.323	1103.200	1091.337	1028.659	933.997	855.290
308.400	1872.207	1845.461	1819.469	1419.586	1404.155	1389.057	1309.280	1188.794	1088.615
416.380	2527.722	2491.612	2456.519	1916.625	1895.792	1875.407	1767.698	1605.026	1469.771
533.800	3240.545	3194.252	3149.262	2457.117	2430.409	2404.275	2266.192	2057.647	1884.250

Table 2. Continued.

$\widetilde{r}$(μm) / λ (μm)	2.1730	2.2100	2.2480	10.2450	10.8000	11.3550	11.4450	12.0000	12.5550
0.700	2.024	1.990	1.957	0.429	0.407	0.387	0.384	0.367	0.350
1.000	2.891	2.843	2.795	0.613	0.582	0.553	0.549	0.524	0.500
1.300	3.759	3.696	3.634	0.797	0.756	0.719	0.714	0.681	0.651
1.900	5.494	5.402	5.311	1.165	1.105	1.051	1.043	0.995	0.951
2.600	7.518	7.392	7.267	1.595	1.513	1.439	1.427	1.361	1.301
3.500	10.120	9.951	9.783	2.147	2.036	1.937	1.921	1.833	1.752
4.900	14.168	13.931	13.696	3.005	2.851	2.711	2.690	2.566	2.452
6.900	19.951	19.617	19.286	4.232	4.014	3.818	3.788	3.613	3.453
9.500	27.469	27.009	26.553	5.826	5.527	5.257	5.215	4.974	4.754
13.200	38.168	37.529	36.894	8.095	7.679	7.304	7.247	6.912	6.606
18.200	52.625	51.744	50.869	11.162	10.588	10.071	9.992	9.529	9.108
25.300	73.154	71.930	70.714	15.516	14.719	14.000	13.889	13.247	12.661
35.100	101.491	99.792	98.105	21.527	20.420	19.422	19.270	18.378	17.566
47.300	1380.103	1356.997	1334.059	292.725	277.682	264.110	262.033	249.914	238.866
60.600	175.224	172.290	169.378	37.166	35.256	33.532	33.269	31.730	30.327
77.100	222.933	219.201	215.495	47.285	44.855	42.663	42.327	40.369	38.585
97.500	281.919	277.199	272.514	59.796	56.723	53.951	53.526	51.051	48.794
122.800	355.074	349.129	343.227	75.312	71.442	67.950	67.416	64.298	61.456
154.000	445.288	437.833	430.432	94.447	89.594	85.214	84.544	80.634	77.070
192.700	557.188	547.860	538.599	118.182	112.108	106.629	105.790	100.897	96.437
242.300	700.606	688.876	677.231	148.601	140.964	134.074	133.020	126.868	121.260
308.400	891.732	876.803	861.981	189.140	179.420	170.650	169.308	161.478	154.340
416.380	1203.954	1183.798	1163.787	255.363	242.240	230.400	228.588	218.016	208.379
533.800	1543.472	1517.631	1491.977	327.376	310.552	295.373	293.051	279.497	267.142

parameters over the PSDs to obtain the bulk scattering properties to be used in the SAD analysis.

$$D_{\text{eff}} = \frac{3}{2}\frac{\int_{D_{\min}}^{D_{\max}} V(D)\, n(D)\, \mathrm{d}D}{\int_{D_{\min}}^{D_{\max}} A(D)\, n(D)\, \mathrm{d}D} = \frac{3}{2}\frac{V_{\text{Tot}}}{A_{\text{Tot}}}, \tag{4}$$

$$\overline{A_{\text{s}}} = \frac{\int_{D_{\min}}^{D_{\max}} A_{\text{s}} n(D)\, \mathrm{d}D}{\int_{D_{\min}}^{D_{\max}} n(D)\, \mathrm{d}D}, \tag{5}$$

$$\overline{g} = \frac{\int_{D_{\min}}^{D_{\max}} g(D,\lambda)\sigma_{\text{sca}}(D,\lambda)\, n(D)\, \mathrm{d}D}{\int_{D_{\min}}^{D_{\max}} \sigma_{\text{sca}}(D,\lambda)\, n(D)\, \mathrm{d}D}, \tag{6}$$

$$\overline{Q_e} = \frac{\int_{D_{\min}}^{D_{\max}} \sigma_{\text{ext}}(D) A(D)\, n(D)\, \mathrm{d}D}{\int_{D_{\min}}^{D_{\max}} A(D)\, n(D)\, \mathrm{d}D}, \tag{7}$$

$$\overline{P}(\theta) = \frac{\int_{D_{\min}}^{D_{\max}} P(\theta, D, \lambda)\, \sigma_{\text{sca}}(D,\lambda)\, n(D)\, \mathrm{d}D}{\int_{D_{\min}}^{D_{\max}} \sigma_{\text{sca}}(D,\lambda)\, n(D)\, \mathrm{d}D}, \tag{8}$$

where $D_{\min}$ and $D_{\max}$ are the minimum and the maximum sizes of the ice particles, and V_{Tot} and A_{Tot} are the total volumes and projected areas of the ice particles, respectively. The parameters A_{s}, g, σ_{sca}, σ_{ext}, and P are the single-scattering albedo, asymmetry factor, scattering cross section, extinction cross section, and phase function, respectively, for a single particle; θ is the scattering angle.

3 Data and methods

Since 1996, three POLDER instruments have been flown to study clouds and aerosols using multiple angles and polarisation capabilities. The POLDER-1 and POLDER-2 instruments aboard JAXA's ADEOS satellite were operated from November 1996 to June 1997 and December 2002 to October 2003, respectively. Both of the POLDER instruments observed intensity from 14 viewing directions, with scattering angles ranging from 60 to 180°. The spatial resolution of the product derived from POLDER-2 observation data is approximately 20 km, which is composed of 3 × 3 single pixels. POLDER-2 measured the upwelling total and polarised radiances from eight observing channels centred at wavelengths of 0.443, 0.490, 0.565, 0.670, 0.763, 0.765, 0.865, and 0.910 μm (Baran and C.-Labonnote, 2006). POLDER-3 operates aboard the Polarization and Anisotropy of Reflectances for Atmospheric Sciences coupled with Observations from a Lidar (PARASOL) microsatellite, launched in 2004. POLDER-3 has nine observing channels, three of which had polarisation capabilities. PARASOL/POLDER-3 views a given scene from up to 16 angles as the satellite passes overhead. However, the capabilities of the instrument, such as observing the radiances from multiple viewing angles in several visible channels, are important for investigating the representative ice particle models for retrieving ice cloud

properties. In this study, 589 × 246 pixels of the POLDER-3 observation data with a global scale, obtained when flying over oceans on 20–22 March, June, September, and December 2008, were used to retrieve cloud optical thickness and spherical albedo in order to investigate the behaviour of the five ice particle habits.

Figure 2a shows the distribution of the number of directional samples used in the SAD analysis. The number of pixels is increased in the scattering angle range of 60 to 160° and is decreased in the scattering angle range from 160 to 180°. There is a peak value of the number of sample pixels in the scattering angle range of 140 to 160°. Figure 2b indicates the variation of the number of pixels by latitude; the number of pixels changes significantly as a function of latitude and is lowest when the latitude is around 90° N and 90° S. There are three peaks of the number of pixels in the different latitudes, due to the location of more samples at midlatitude, where storm tracks occur, as well as along the Intertropical Convergence Zone (ITCZ), where there are numerous deep convective clouds. C.-Labonnote et al. (2000) and Baran and C.-Labonnote (2006) proposed the SAD method for testing the phase function of the various ice particle models, using POLDER observational data with multiple viewing angles. For investigating the phase functions (P_{11}) of the different ice crystal models for retrieving the cloud microphysical properties, the cloud spherical albedo as a function of scattering angle is required. For calculating the cloud spherical albedo, bidirectional reflection is first determined by

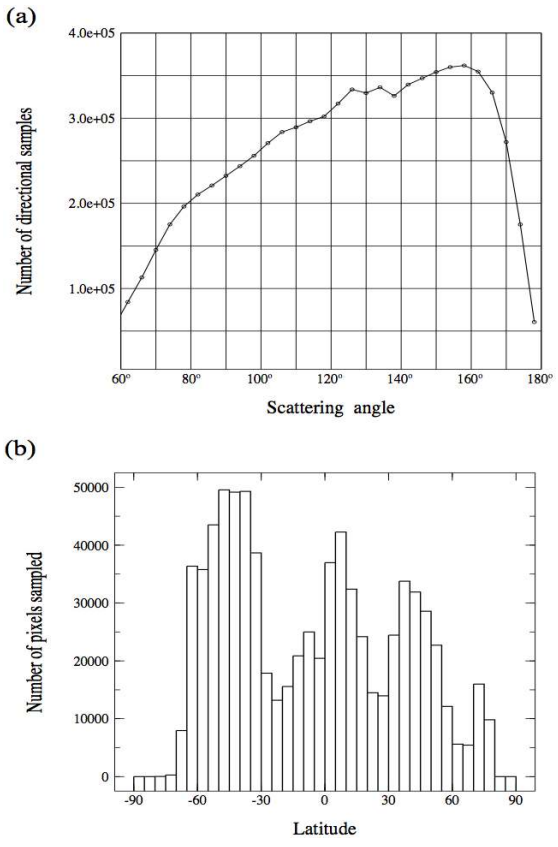

Figure 2. (a) Angular distribution and **(b)** latitude distribution of the sample pixels.

$$R_{\mathrm{cld}}(\mu, \mu_0, \phi - \phi_0) = \pi L_{\mathrm{obs}}(\mu\mu_0\phi - \phi_0)/\mu_0 F_0, \tag{9}$$

where u and u_0 are cosines of the satellite and solar zenith angles, $\phi - \phi_0$ is the relative azimuth angle between the satellite and the sun, L_{obs} is the reflected solar radiance observed by the satellite, and F_0 is the solar flux density. POLDER usually observes a given Earth target (pixel) under up to 16 different directions. From each of these N observations a so-called "directional cloud optical thickness" is retrieved from L_{obs} using pre-computed LUTs that provide the bidirectional reflection (R_{lcd}) of clouds as a function of optical thickness, zenith angles, and relative azimuth angle. The cloud-plane albedo (A_{p}) and spherical albedo (S) are calculated by integrating over all the zenith and azimuth angles as

$$A_{\mathrm{p}}(\mu_0) = \iint R_{\mathrm{cld}}(\mu, \mu_0, \phi - \phi_0)\mu \mathrm{d}\mu \mathrm{d}\phi, \tag{10}$$

$$S = \int A_{\mathrm{p}}(\mu_0)\mu_0 \mathrm{d}\mu_0. \tag{11}$$

A total of N observation of L_{obs} are acquired under different viewing geometries hence associated with different scattering angles θ. Those are converted to N directional optical thickness values which in turn can be translated into equivalent direction spherical albedo values using Eqs. (9) to (11).

Eventually we obtain N values of cloud spherical albedo S for various θ values. Baran and C.-Labonnote (2006) assumed that if the scattering phase function of the ice particle model is correct, then calculated $S(\theta)$ in each direction should be the same and the SAD, as shown in Eq. (13), should be 0. $\overline{S}$, SAD, and θ are given as

$$\overline{S} = (1/N)\sum S(\theta), \tag{12}$$

$$\mathrm{SAD} = S(\theta) - \overline{S}, \tag{13}$$

$$\cos\theta = \cos(\pi - u_0)\cos u + \sin u_0 \sin u \cos(\phi - \phi_0), \tag{14}$$

where u_0 and u are the solar and satellite zenith angles, respectively.

The steps for applying the SAD analysis to POLDER-3 measurements are as follows:

1. Calculate spherical albedo from the POLDER-3 measurements with 16 viewing geometries for each of the ice particle models.
2. Perform the SAD analysis by taking the difference between the directional and the direction-averaged cloud spherical albedo.
3. Assume that the phase function for each ice particle model adequately represents the phase function for all

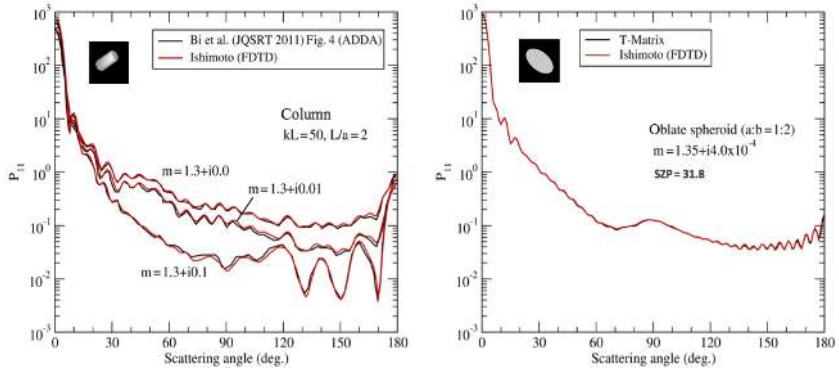

Figure 3. Comparison of the phase functions of randomly oriented column and spheroid particle from FDTD, T-matrix, and ADDA methods.

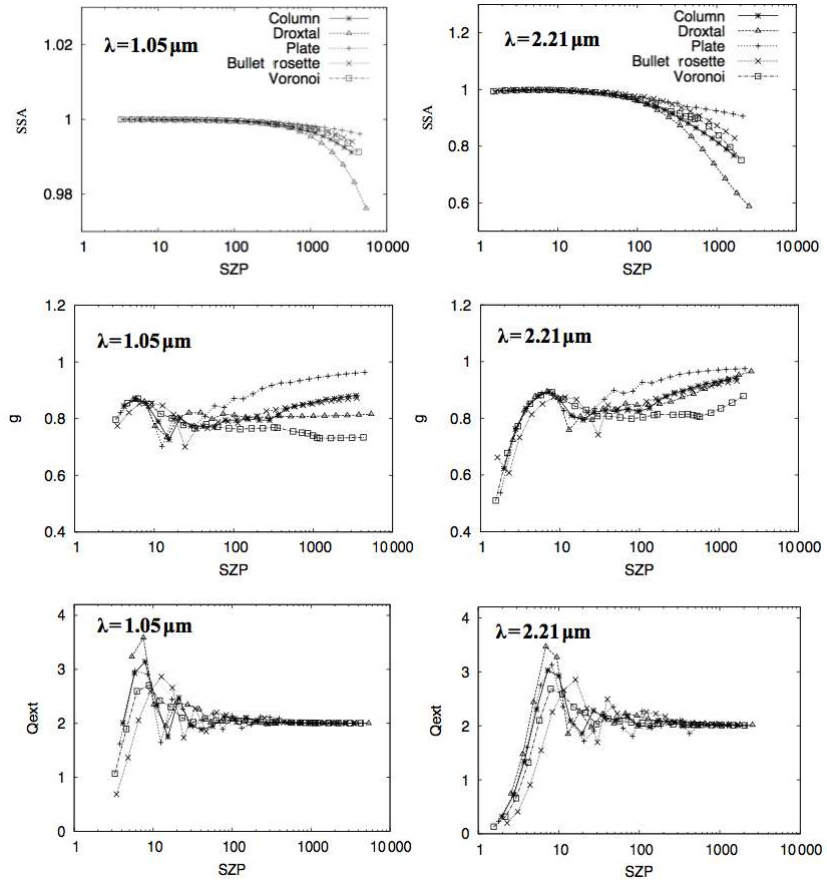

Figure 4. Comparison of the single-scattering property of the various ice crystals models computed in this study at wavelength of 1.05 and 2.21 µm (SSA: single-scattering albedo; g: asymmetry factor; Q_{ext}: extinction efficiency).

ice particles in each pixel of the satellite measurement and that the retrievals of the optical thickness and spherical albedo from the POLDER measurements with different viewing geometries are the same.

When the SAD is 0, the mean spherical albedo and the spherical albedo from the specific angle of POLDER-3 measurements are the same. Therefore, the criteria for selecting the optimal particle habit of the ice cloud are defined as an SAD near 0 in the 16 viewing geometries of POLDER-3 and a small angular dependence.

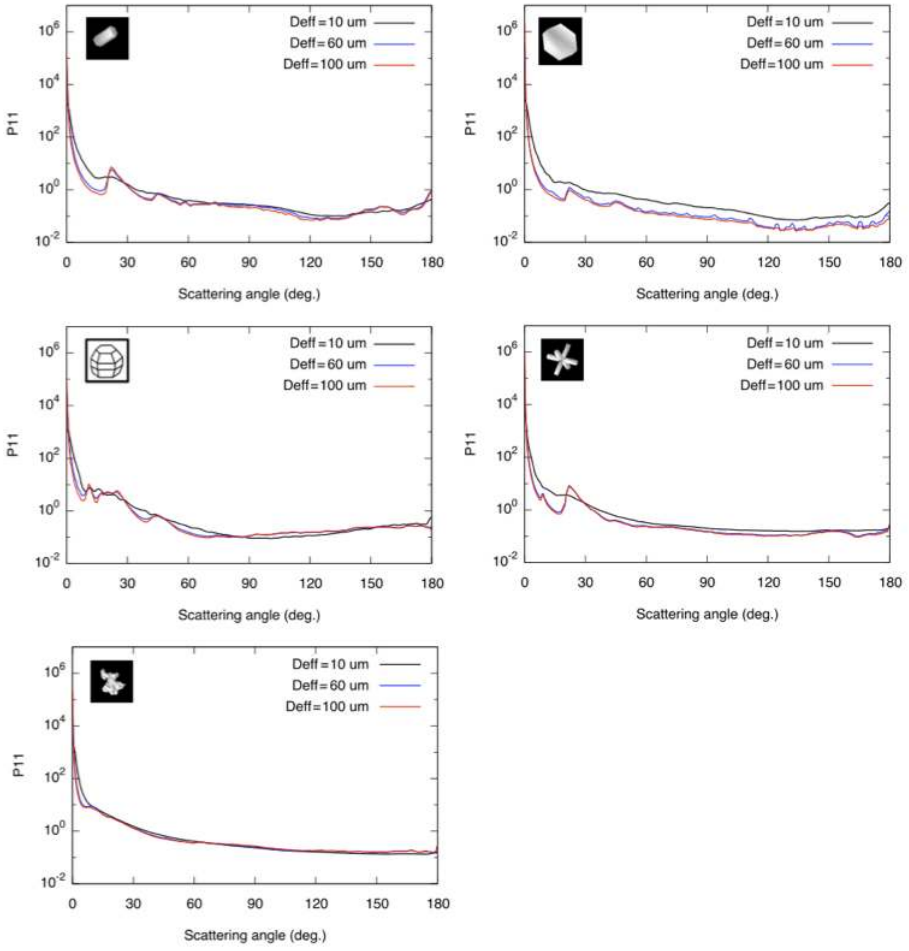

Figure 5. Bulk scattering phase functions of the column, droxtal, plate, bullet rosette, and Voronoi habit employed in this study with various effective diameters at wavelengths of 1.05 µm.

4 Results and discussion

4.1 Characteristics of the scattering properties

To confirm the accuracy of the calculated single-scattering properties, the phase functions computed in this study are compared with other results. Figure 3 shows comparisons of the phase function (P_{11}) of hexagonal and spheroid particles calculated from the FDTD method with those derived from the ADDA (Bi et al., 2011) and T-matrix methods, respectively. Our FDTD results are the same as those calculated with the other methods. In addition, the results of Ishimoto et al. (2012b) and Masuda et al. (2012) verify that the phase functions of ice particles with medium and large size parameters are the same through a comparison of the GOIE and GOM results, respectively.

The single-scattering albedo, asymmetry factor, and extinction efficiency among the key parameters of the single-scattering properties of ice particles. Figure 4 shows the single-scattering properties of various ice particle habits at wavelengths of 1.05 and 2.2 µm for various size parameters. The value of the single-scattering albedo is close to 1.0 when size parameters are less than approximately 200 at wavelength 1.05 µm and 50 at wavelength 2.2 µm; the value decreases with increasing values of the size parameter. There is a smooth peak in the asymmetry factor for size parameters of 1 to 10, and the peak of the asymmetry factor at a wavelength of 2.1 µm is larger than that at 1.05 µm. The asymmetry factor does not increase monotonically because, due to the complex shapes of the Voronoi habit, the effect of side and back scattering is significant. This results in the asymmetry factor of the Voronoi model being smaller than that of the plate and solid column models. Furthermore, due to the absorption inside the particles, the side-back scattering and single-scattering albedo decreases with the increasing particle size. This results in the asymmetry factor increasing. Absorption of the ice particle in the wavelength of 1.05 µm is not so large, and as a result, the asymmetry factor of the Voronoi particle does not increase monotonically. The extinction efficiency increases with the size parameter for size parameters

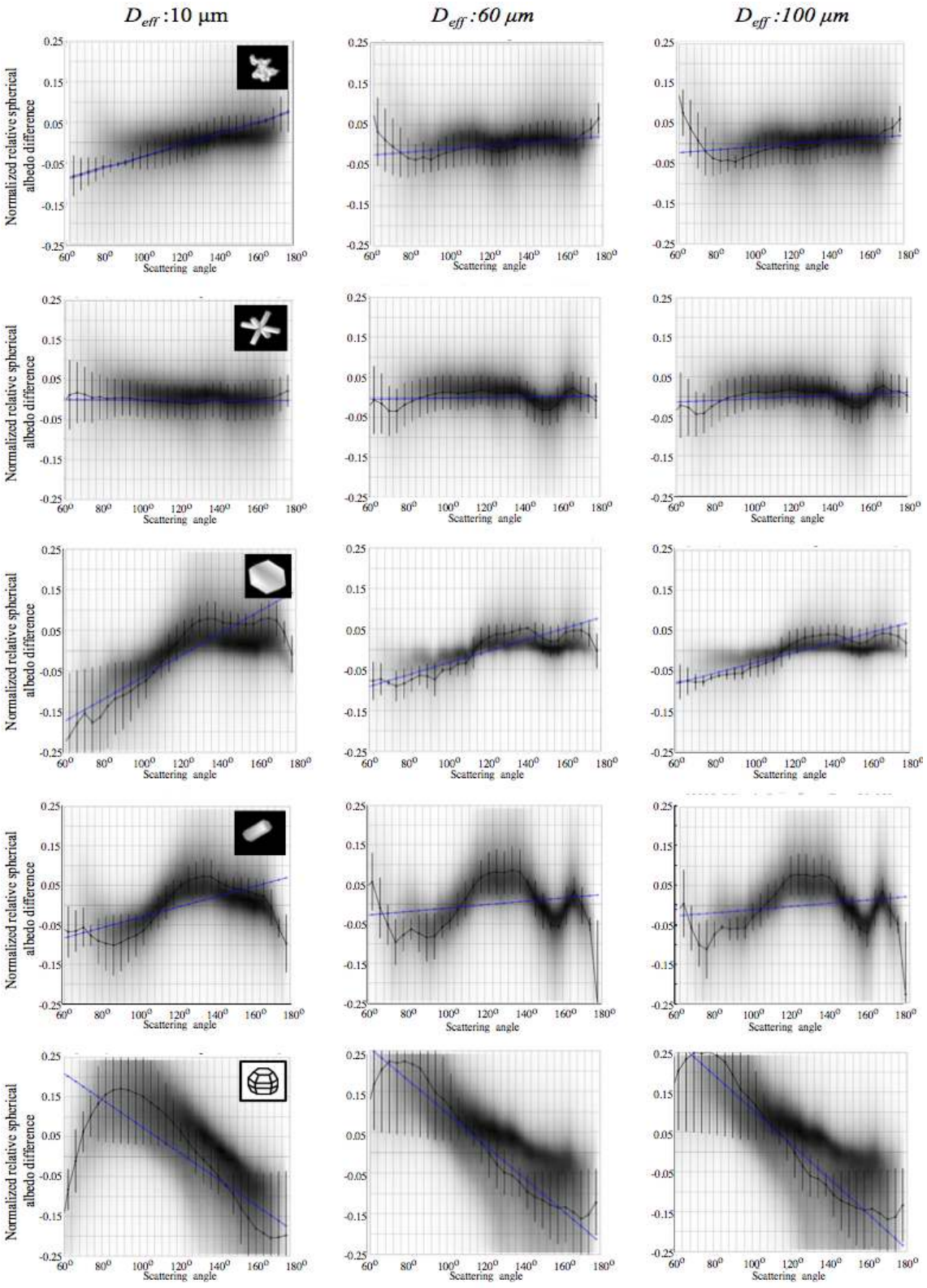

Figure 6. SAD analysis as a function of different particle habits and effective diameters (D_{eff}) using POLDER measurement. Black contours show the density of the observations normalised to the maximum value, and the blue line shows the regression line.

up to approximately 10 and converges gradually to 2 when the size parameter exceeds 100. The maximum values of extinction efficiency appear when the size parameter is around 10. However, the location of the maximum extinction efficiency varies with particle habit.

Bulk scattering phase functions of the column, droxtal, plate, bullet-rosette, and Voronoi habits, with various effective diameters at wavelengths of 1.05 µm, are given in Fig. 5. The phase functions depend on the particle habit and effective diameters. There is a halo peak for the column, plate, and bullet-rosette habits when effective diameters are 60 and 100 µm, as particle roughening is not applied in these calculations. For the droxtal, variation of the phase function is evident for different effective diameters. The POLDER-3 measures intensity from 16 viewing directions at scattering angles between 60 and 180°; for these scattering angles, the phase function curves of the various particles are different. The phase function of the Voronoi habit is very smooth, with features similar to those for severely roughened ice particle models and the IHM model, except for the halo peak region, as reported by Yang et al. (2013) and Doutriaux-Boucher et al. (2000).

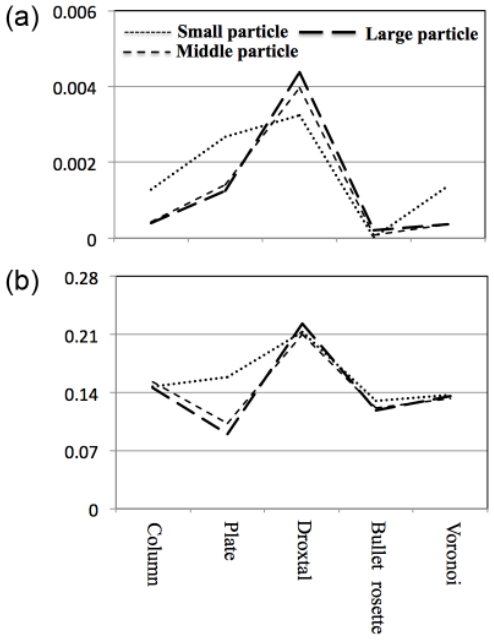

Figure 7. The slope of the regression function and total relative albedo difference in Fig. 6.

4.2 SAD analysis

Figure 6 shows the SAD analysis as a function of the scattering angle, effective particle radius, and ice particle models. The SAD of the droxtal, column, and plate shows substantial variations in both the scattering angle and effective particle radius. The variation of SAD for the bullet-rosette model is more smoothly distributed close to 0 value of the SAD (hereafter, "zero line") than with the droxtal, plate, and column models for small ($D_{\mathrm{eff}} = 10\,\mu\mathrm{m}$), medium ($D_{\mathrm{eff}} = 60\,\mu\mathrm{m}$), and large particles ($D_{\mathrm{eff}} = 100\,\mu\mathrm{m}$). However, the SAD peak of the bullet-rosette model varies in the scattering angle range of 140 to 160° with medium and large particles. The SAD of the Voronoi model is closest to the zero line over the entire scattering angle range for small, medium, and large particles. Both the Voronoi and bullet-rosette model with small particles are smoothly distributed along the zero line.

Figure 7 shows the slope of the regression function (SRF) and total relative albedo difference (TRAD) of the SAD for the same five ice particle models with small, medium, and large particles, as shown in Fig. 6. Values of both the SRF and TRAD for small particles of the bullet rosette, and for medium and large particles of the bullet rosette and Voronoi, are the smallest of all the single-particle models considered. However, there is a peak value of the SAD in the scattering angle range of 140 to 160° for the bullet-rosette model with medium and large particles. The SRF and TRAD of the droxtal model for all sizes of particles are largest in all habit models. As we have described in Sect. 3, the optimal particle habit is defined as the smallest value of the SRF and TRAD. Thus, it was confirmed that the bullet-rosette model with small particles and Voronoi model with medium and large particles are sufficiently accurate for the retrieval of the ice cloud spherical albedo and optical thickness. Therefore, these models are sufficient to represent ice clouds in terms of optimal particle habits for the purposes of the SGLI sensor.

Ice crystals in ice clouds are complex. To simulate this complexity, we assume different values of distortion (as defined by Macke et al., 1996b) and apply these to the ensemble model. Numerous previous studies have shown that the degree of distortion is an important property to consider when retrieving ice cloud optical properties from multiple-view instruments. To investigate the influence of the distortion of the ice particle model on retrieval of the ice cloud properties, we performed the SAD analysis using the ensemble ice particle models with $D_{\mathrm{eff}} = 60\,\mu\mathrm{m}$, assuming a number of distortion values (see Fig. 8). The variation of SAD for the no-distortion model in Fig. 8a is largest relative to the other distortion values. As a function of distortion value, there are significant variations in the SAD analysis in the scattering angle ranges of 60 to 80° and 140 to 160°. There is no obvious difference in the SAD between Fig. 8b, c, and d for various degrees of the distortions. The SAD of the ice particle models with a distortion value of 0.4 with spherical air bubbles in Fig. 8e is closest to the zero line. It is implied that the models with distortion or surface roughness are better for the retrieval of the ice cloud optical properties than if no distortion were applied to the model. The models that include spherical air bubbles and distortion have lower SAD values than models with distortion only.

Several conventional studies have demonstrated that ice particle models such as the ensemble ice particle model,

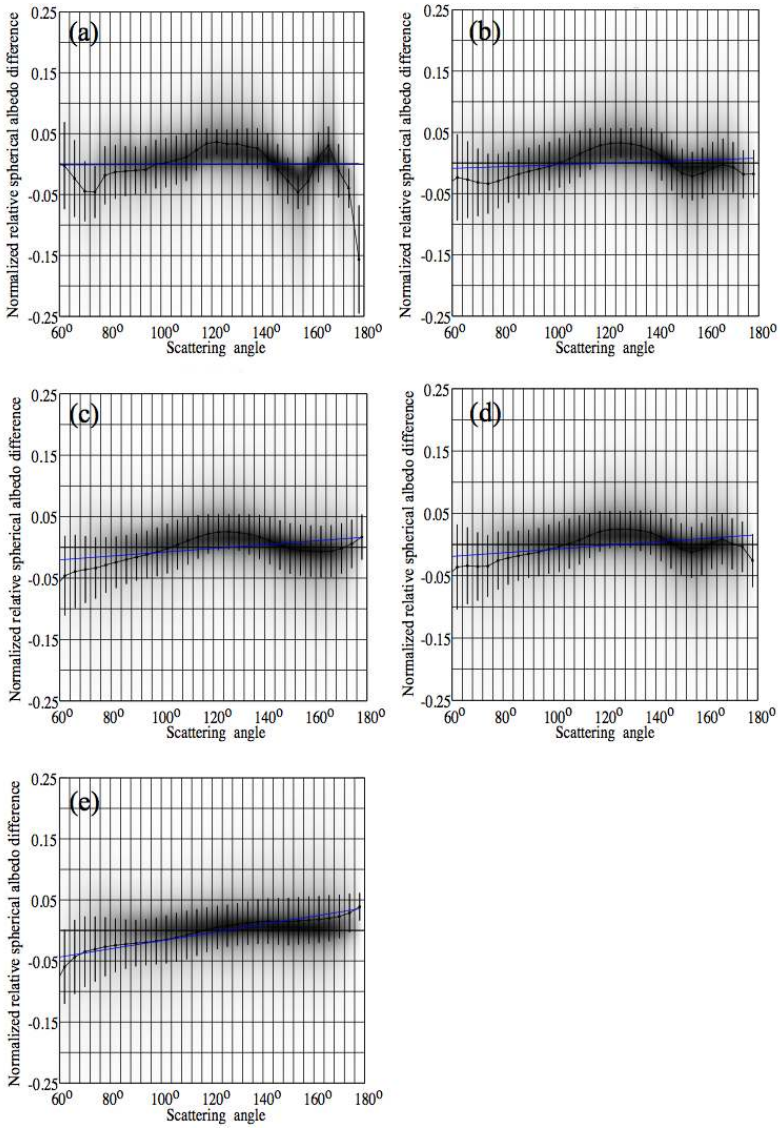

Figure 8. SAD analysis of the ensemble ice particle model with $D_{\text{eff}} = 60\,\mu\text{m}$ for various distortions: **(a)** no distortion applied; **(b)** with distortion value of 0.15; **(c)** with distortion value of 0.25; **(d)** averaged over all distortion values; **(e)** distortion value of 0.4 is assumed with spherical air inclusions.

IHM, and GHM, as well as some aggregated complex models with rough surfaces, are useful for operational satellite data processing (C.-Labonnote et al., 2000, 2001; Doutriaux-Boucher et al., 2000; Baum et al., 2011, 2014; Baran and C.-Labonnote, 2006, 2007; Cole et al., 2013). For evaluating the accuracy of the Voronoi model, the SAD of the Voronoi model is compared with that of the conventional IHM, GHM, five-plate aggregate, and ensemble ice particle models with $D_{\text{eff}} = 60\,\mu\text{m}$. As shown in Fig. 9, none of the selected models have strong angular dependencies. However, all the models in Fig. 9 have a rough surface except for the IHM, which contains spherical air bubbles, and the Voronoi habit. This implies that the Voronoi habit model has a similar effect as some aggregated and mixed-habit ice particle models with roughened surfaces, and the IHM single-particle model contains air bubbles on retrieval of the ice cloud properties using remote sensing instruments. This conclusion is consistent with the conclusion of Liu et al. (2014b), which states that geometric irregularity and surface roughness are effectively equivalent.

Figure 10 shows the slope of the regression function (top panel) and total relative albedo difference (bottom panel) for the selected models in Fig. 9. The SRF for the GHM, Voronoi, and averaged-ensemble models is significantly smaller than for the other three models. The TRAD values for each habit model are not significantly different. However, the TRAD value obtained for the Voronoi model is slightly smaller than the other models, except for

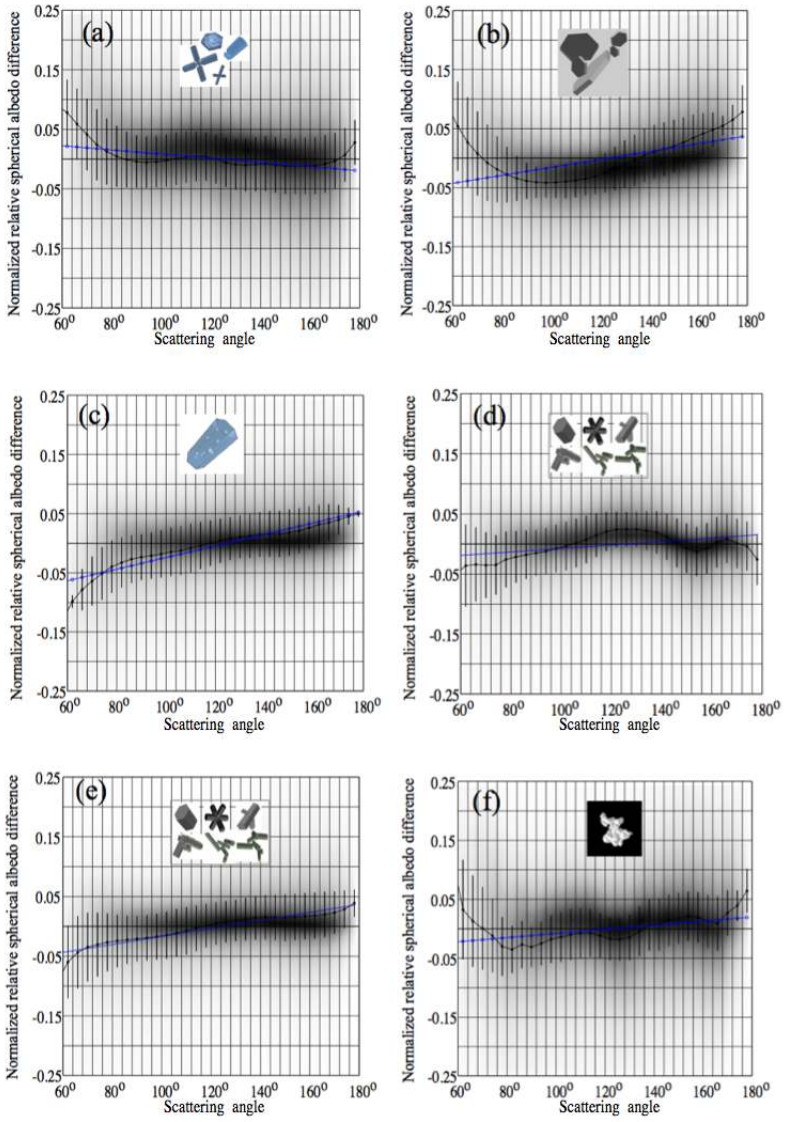

Figure 9. Comparison of the SAD analysis for various ice particle models with **(a)** $D_{\mathrm{eff}} = 60\,\mu\mathrm{m}$, GHM model with rough surface; **(b)** 5-plate_agr, five-plate aggregate model with rough surface; **(c)** IHM model with smooth surface; **(d)** Ensemble_ave, ensemble ice particle model with averaged over all distortion value; **(e)** Ensemble_0.4, ensemble ice particle model by assuming a distortion value of 0.4 with spherical air inclusions; and **(f)** Voronoi model.

the averaged-ensemble ice particle model. The Voronoi and averaged-ensemble models have small values of SRF and TRAD, indicating that the SAD of the Voronoi and averaged-ensemble models have a low angular dependence.

5 Conclusions

Ice particle single-scattering properties were investigated for potential use in the GCOM-C satellite programme. The single-scattering properties of five different ice particle models (plates, columns, droxtals, bullet rosettes, and Voronoi) were developed using the FDTD, GOIE, and GOM methods. The accuracy of the single-scattering property was investigated by comparing the phase function from the FDTD method used in this study with conventional results from ADDA and T-matrix methods. The FDTD phase functions were also compared with computational results from GOIE. Results indicate that the FDTD-based phase functions are consistent with results from the ADDA, T-matrix, and GOIE methods, which suggests that the single-scattering property database developed in this study is reliable for use in radiative transfer simulations and applications in the remote sensing of ice clouds.

The characteristics of the single-scattering property database for five different ice particle models were investi-

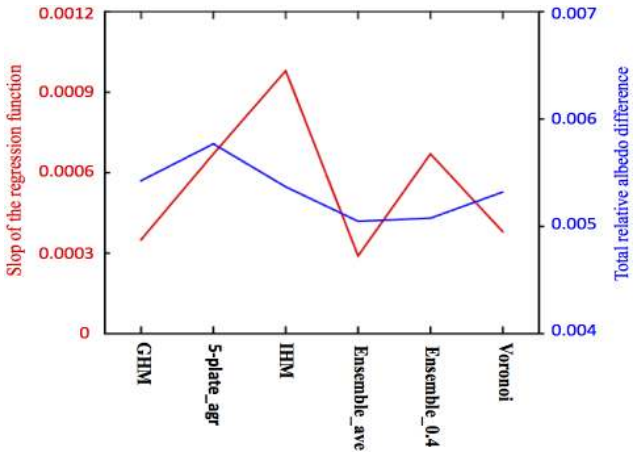

Figure 10. The slope of the regression function and total relative albedo difference for various ice particle models in Fig. 9.

gated by analysing the single-scattering albedo, asymmetry factor, and the extinction efficiency. Bulk scattering phase functions for five different ice particle models at the wavelength of 1.05 µm were compared as a function of various effective diameters. It is concluded that phase functions depend on the particle habit and effective diameters. There is a halo peak for middle and large sizes of column, plate, and bullet-rosette habits. For the droxtal particle, variation of the phase function is evident for different effective diameters. The phase function of the Voronoi habit is very smooth, with features similar to those of severely roughened ice particle models.

Furthermore, SAD analysis was performed to determine the optimal ice particle habit for retrieving the optical thickness and cloud spherical albedo using POLDER-3 multi-angle measurements. Retrievals were performed using 589×246 pixels of the POLDER-3 observation data on a global scale, recorded over oceans on 20–22 March, June, September, and December 2003. The following conclusions are drawn from the results.

1. The SADs of the droxtal and column habits show significant variations in scattering angle and effective particle radius.
2. SAD variation for small particles with the bullet-rosette model is more smoothly distributed along the zero line than that with other habit models.
3. The Voronoi model SAD is closest to the zero line in scattering angle for all particle sizes.
4. The bullet-rosette habit for small particles and the Voronoi habit for all particle sizes are most suitable for retrieving the ice cloud spherical albedo and optical thickness.

In other words, results of the SAD analysis indicate that the Voronoi particle has scattering characteristics that are useful for retrievals, e.g. agreement with POLDER/PARASOL polarised reflectances, a low asymmetry parameter, and a smooth phase function. Furthermore, the results of SAD analysis from the Voronoi model were compared with results from the conventional IHM, GHM, five-plate aggregate, and ensemble ice particle models with moderate ice particle size in order to evaluate the efficiency of the Voronoi model. It is concluded that the Voronoi habit model is similar to the conventional models for retrieval of ice cloud properties with thick optical thickness, using remote sensing instruments. The results of this study should be useful not only for developing the ice cloud products of the GCOM-C/SGLI satellite mission but also for determining the optimal ice particle habit for ice cloud remote sensing. In future work, we will compare the optical properties derived from the Voronoi model and the severely roughened aggregated columns model used in MODIS Collection 6 ice cloud algorithm. We will also investigate how the Voronoi particle behaves at low optical thickness values, in direct comparison with the retrievals from CALIPSO/CALIOP polarisation lidar data.

6 Data availability

Data are available upon request.

Acknowledgements. This work was supported by the GCOM-C/SGLI and EarthCARE project of the Japan Aerospace Exploration Agency (JAXA), the Japan Science and Technology Agency (JST), CREST/EMS/TEEDDA, CAS Pioneer Hundred Talents Program (Y6YR0600QM), and National Natural Science Foundation of China (61261030). The authors would like to thanks ICARE and CNES for providing the POLDER data as well as François Thieuleux for his support with POLDER data analysis. The authors gratefully acknowledge Bryan A. Baum (UW-Madison) for providing the GHM ice particle model.

Edited by: J.-Y. C. Chiu
Reviewed by: B. Baum and one anonymous referee

References

Baran, A. J. and C.-Labonnote, L.: On the reflection and polarization properties of ice cloud, J. Quant. Spectrosc. Ra., 100, 41–54, 2006.

Baran, A. J. and C.-Labonnote, L.: A ensemble ice particle scattering model for cirrus, I: The solar region, Q. J. Roy. Meteor. Soc., 133, 1899–1912, 2007.

Baran, A. J., Watts, P. D., and Foot, J. S.: Potential retrieval of dominating crystal habit and size using radiance data from a dual-view and multiwavelength instrument: A tropical cirrus anvil case, J. Geophys. Res., 103, 6075–6082, 1998.

Baran, A. J., Watts, P. D., and Francis, P. N.: Testing the coherence of cirrus microphysical and bulk properties retrieved from dual-viewing multispectral satellite radiance measurements, J. Geophys. Res., 104, 31673–31683, 1999.

Baran A. J., Francis, P. N., Labonnote, L. C., and Doutriaux-Boucher, M.: A scattering phase function for ice cloud: Tests of applicability using aircraft and satellite multi-angle multiwavelength radiance measurements of cirrus, Q. J. Roy. Meteorol. Soc., 127, 2395–2416, 2001.

Baran, A. J., Havemann, S., Francis, P. N., and Watts, P. D.: A consistent set of single-scattering properties for cirrus cloud: tests using radiance measurements from a dual-viewing multi-wavelength satellite-based instrument, J. Quant. Spectrosc. Ra., 79–80, 549–567, 2003.

Baran, A. J., Hill, P., Furtado, K., Field, P., and Manners, J.: A Coupled Cloud Physics–Radiation Parameterization of the Bulk Optical Properties of Cirrus and Its Impact on the Met Office Unified Model Global Atmosphere 5.0 Configuration, J. Climate, 27, 7725–7752, 2014.

Baum, B. A., Yang, P., Heymsfield, A. J., Platnick, S., King, M. D., and Bedka, S. T.: Bulk scattering models for the remote sensing of ice clouds. Part 2: Narrowband models, J. Appl. Meteorol., 44, 1896–1911, 2005.

Baum, B. A., Yang, P., Heymsfield, A. J., Schmitt, C., Xie, Y., Bansemer, A., Hu, Y.-X., and Zhang, Z.: Improvements to shortwave bulk scattering and absorption models for the remote sensing of ice clouds, J. Appl. Meteorol. Clim., 50, 1037–1056, 2011.

Baum, B. A., P. Yang, A. J. Heymsfield, A. Bansemer, B. H. Cole, A. Merrelli, C. Schmitt, and Wang, C.: Ice cloud single-scattering property models with the full phase matrix at wavelengths from 0.2 to 100 µm, J. Quant. Spectrosc. Ra., 146, 123–139, 2014.

Bi, L. and Yang, P.: High-frequency extinction efficiencies of spheroids: rigorous T-matrix solutions and semi-empirical approximations, Opt. Express, 22, 10270–10293, 2014a.

Bi, L. and Yang, P.: Accurate simulation of the optical properties of atmospheric ice crystals with invariant imbedding T-matrix method, J. Quant. Spectrosc. Ra., 138, 17–35, 2014b.

Bi, L., Yang, P., and Kattawar, G. W.: Edge-effect contribution to the extinction of light by dielectric disk and cylindrical particles, Appl. Optics, 49, 4641–4646, 2010.

Bi, L., Yang, P., Kattawar, G. W., Hu, Y., and Baum, B. A.: Scattering and absorption of light by ice particles: solution by a new physical-geometric optics hybrid method, J. Quant. Spectrosc. Ra., 112, 1492–1508, 2011.

Chen, G., Yang, P., and Kattawar, G. W.: Application of the pseudospectral time-domain method to the scattering of light by nonspherical particles, J. Opt. Soc. Am. A, 25, 785–90, 2008.

Chepfer, H., Brogniez, G., and Fouquart, Y.: Cirrus clouds' microphysical properties deduced from POLDER observations, J. Quant. Spectrosc. Ra., 60, 375–390, 1998.

Chepfer, H., Goloub, P., Riedi, J., de Haan, J. F., and Hovenier, J. W.: Ice crystal shapes in cirrus clouds derived from POLDER-1/ADEOS-1, J. Geophys. Res., 106, 7955–7966, doi:10.1029/2000JD900285, 2001.

Chepfer, H., Minnis, P., Young, D., Nguyen, L., and Arduini, R. F.: Estimation of cirrus cloud effective ice crystal shapes using visible reflectances from dual-satellite measurements, J. Geophys. Res., 107, 4730, doi:10.1029/2000JD000240, 2002.

C.-Labonnote, L., Brogniez, G., Doutriaux-Boucher, M., Buriez, J. C., Gayet, J. F., and Chepfer, H.: Modeling of light scattering in cirrus clouds with inhomogeneous hexagonal monocrystals. Comparison with in-situ and ADEOS-POLDER measurements, Geophys. Res. Lett., 27, 113–116, 2000.

C.-Labonnote, L., Brogniez, G., Buriez, J. C., and Doutriaux-Boucher, M.: Polarized light scattering by inhomogeneous hexagonal monocrystals: validation with ADEOS-POLDER measurements, J. Geophys. Res., 106, 12139–12153, 2001.

Cole, B., Yang, P., Baum, B. A., Riedi, J., C.-Labonnote, L., Thieuleux, F., and Platnick, S.: Comparison of PARASOL observations with polarized reflectances simulated using different ice habit mixtures, J. Appl. Meteorol. Clim., 52, 186–196, 2013.

Cole, B. H., Yang, P., Baum, B. A., Riedi, J., and C.-Labonnote, L.: Ice particle habit and surface roughness derived from PARASOL polarization measurements, Atmos. Chem. Phys., 14, 3739–3750, doi:10.5194/acp-14-3739-2014, 2014.

Doutriaux-Boucher, M., Buriez, J. C., Brogniez, G., Labonnote, L. C., and Baran, A. J.: Sensitivity of retrieved POLDER directional cloud optical thickness to various ice particle models, Geophys. Res. Lett., 27, 109–112, 2000.

Draine, B. T. and Flatau, P. J.: Discrete-dipole approximation for scattering calculations, J. Opt. Soc. Am. A, 11, 1491–1499, 1994.

Foot, J. S.: Some observations of the optical properties of clouds. II: Cirrus, Q. J. Roy. Meteor. Soc., 114, 145–164, 1988.

Forster, P., Ramaswamy, V., Artaxo, P., Berntsen, T., Betts, R., Fahey, D., Haywood, J., Lean, J., Lowe, D., Myhre, G., Nganga, J., Prinn, R., Raga, G., Schulz, M., and Van Dorland, R.: Changes in Atmospheric Constituents and in Radiative Forcing, in: IPCC Fourth Assessment Report WG 1, edited by: Solomon, S., Qin, D., Manning, M., Chen, Z., Marquis, M., Averyt, K. B., Tignor, M., and Miller, H. L., Cambridge University Press, Cambridge, UK, 129–234, 2007.

Groth, S. P., Baran, A. J., Betcke, T., Havemann, S., and Śmigaj, W.: The boundary element method for light scattering by ice crystals and its implementation in BEM++, J. Quant. Spectrosc. Ra., 167, 40–52, doi:10.1016/j.jqsrt.2015.08.001, 2015.

Hess, M. and Wiegner, M.: COP: A data library of optical properties of hexagonal ice crystals, Appl. Optics, 33, 7740–7746, 1994.

Heymsfield, A. J.: Properties of Tropical and Midlatitude Ice cloud Particle Ensembles. Part I: Median Mass Diameters and Terminal Velocities, J. Atmos. Sci., 60, 2573–2591, 2003.

Heymsfield, A. J., Bansemer, A., Field, P. R., Durden, S. L., Stith, J. L., Dye, J. E., Hall, W., and Grainger, C. A.: Observations and Parameterizations of Particle Size Distributions in Deep Tropical Cirrus and Stratiform Precipitating Clouds: Results from In Situ Observations in TRMM Field Campaigns, J. Atmos. Sci., 59, 3457–3491, 2002.

Heymsfield, A. J., Schmitt, C., and Bansemer, A.: Ice cloud particle size distributions and pressure dependent terminal velocities from in situ observations at temperatures from 0° to −86 °C, J. Atmos. Sci., 70, 4123–4154, 2013.

Holz, R. E., Platnick, S., Meyer, K., Vaughan, M., Heidinger, A., Yang, P., Wind, G., Dutcher, S., Ackerman, S., Amarasinghe, N., Nagle, F., and Wang, C.: Resolving ice cloud optical thickness biases between CALIOP and MODIS using infrared retrievals, Atmos. Chem. Phys., 16, 5075–5090, doi:10.5194/acp-16-5075-2016, 2016.

Imaoka, K., Kachi, M., Fujii, H., Murakami, H., Hori, M., Ono, A., and Shimoda, H.: Global Change Observation Mission (GCOM) for monitoring carbon, water cycles, and climate change, Proceedings of the IEEE, 98, 717–734, 2010.

Ishimoto, H., Masuda, K., Mano, Y., Orikasa, N., and Uchiyama, A.: Optical modeling of irregularly shaped ice particles in con-

vective cirrus, in: Radiation processed in the atmosphere and ocean (IRS2012): Proceedings of the International Radiation Symposium (IRC/IAMAS) 1531, 184–187, 2012a.

Ishimoto, H., Masuda, K., Mano, Y., Orikasa, N., and Uchiyama, A.: Irregularly shaped ice aggregates in optical modeling of convectively generated ice clouds, J. Quant. Spectrosc. Ra., 113, 632–643, 2012b.

Knap, W. H., C.-Labonnote, L., Brogniez, G., and Stammes, P.: Modeling total and polarized reflectances of ice clouds: Evaluation by means of POLDER and ATSR-2 measure- ments, Appl. Optics, 44, 4060–4073, 2005.

Letu, H., Nakajima, T. Y., and Matsui, T. N.: Development of an ice crystal scattering database for the global change observation mission/second generation global imager satellite mission: Investigating the refractive index grid system and potential retrieval error, Appl. Optics, 51, 6172–6178, 2012.

Liou, K. N.: Influence of Cirrus Clouds on Weather and Climate Processes: A Global Perspective, Mon. Weather Rev., 114, 1167–1199, 1986.

Liu, C., Panetta, R. L., and Yang, P.: Application of the pseudospectral time domain method to compute particle single-scattering properties for size parameters up to 200, J. Quant. Spectrosc. Ra., 113, 1728–1740, 2012.

Liu, C., Yang, P., Minnis, P., Loeb, N., Kato, S., Heymsfield, A., and Schmitt, C.: A two-habit model for the microphysical and optical properties of ice clouds, Atmos. Chem. Phys., 14, 13719–13737, doi:10.5194/acp-14-13719-2014, 2014a.

Liu, C., Panetta, R. L., and Yang, P.: The effective equivalence of geometric irregularity and surface roughness in determining particle single-scattering properties, Opt. Express, 22, 23620–23627, doi:10.1364/OE.22.023620, 2014b.

Liu, Q. H.: The PSTD algorithm: a time-domain method requiring only two cells per wavelength, Microwave Opt. Technol. Lett., 15, 158–165, 1997.

Liu, Q. H.: The pseudospectral time-domain (PSTD) algorithm for acoustic waves in absorptive media, IEEE Trans. Ultrason. Ferroelectr. Freq. Control, 45, 1044–1055, 1998.

Macke, A.: Scattering of light by polyhedral ice crystals, Appl. Optics, 32, 2780–2788, 1993.

Macke, A., Mishchenko, M. I., and Cairns, B.: The influence of inclusions on light scattering by large ice particles, J. Geophys. Res., 101, 23311–23316, 1996a.

Macke, A., Mueller, J., and Raschke, E.: Single Scattering Properties of Atmospheric Ice Crystals, J. Atmos. Sci., 53, 2813–2825, 1996b.

Mano, Y.: Exact solution of electromagnetic scattering by a three-dimensional hexagonal ice column obtained with the boundary-element method, Appl. Optics, 39, 5541–5546, 2000.

Masuda, K., Ishimoto, H., and Takashima, T.: Retrieval of cirrus optical thickness and ice-shape information using total and polarized reflectance from satellite measurements, J. Quant. Spectrosc. Ra., 75, 39–51, 2002.

Masuda, K., Ishimoto, H., and Mano, Y.: Efficient method of computing a geometric optics integral for light scattering, Meteorology and Geophysics, 63, 15–19, 2012.

McFarquhar, G. M. and Heymsfield, A. J.: Microphysical characteristics of three anvils sampled during the Central Equatorial Pacific Experiment, J. Atmos. Sci., 53, 2401–2423, 1996.

Nakajima, T. Y., Nakajima, T., Yoshimori, K., Mishra, S. K., and Tripathi, S. N.: Development of a light scattering solver applicable to particles of arbitrary shape on the basis of the surface integral equations method of Muller-type (SIEM/M): Part I. Methodology, accuracy of calculation, and electromagnetic current on the particle surface, Appl. Optics, 48, 3526–3536, 2009.

Nakajima, T. Y., Tsuchiya, T., Ishida, H., Matsui, T. N., and Shimoda, H.; Cloud detection performance of spaceborne visible-to-infrared multispectral imagers, Appl. Optics, 50, 2601–2616, 2011.

Nousiainen, T., Lindqvist, H., McFarquhar, G. M., and Um, J.: Small irregular ice crystals in tropical cirrus, J. Atmos. Sci., 68, 2614–2627, doi:10.1175/2011JAS3733.1, 2011.

Ohser, J. and Mücklich, F.: Statistical analysis of microstructures in materials science, Chichester, England: Wiley, 2000.

Ottaviani, M., Cairns, B., Chowdhary, J., van Diedenhoven, B., Knobelspiesse, K., Hostetler, C., Ferrare, R., Burton, S., Hair, J., Obland, M., and Rogers, R.: Polarimetric retrievals of surface and cirrus clouds properties in the region affected by the deep-water horizon oil spill, Remote Sens. Environ., 121, 389–403, doi:10.1016/j.rse.2012.02.016, 2012.

Purcell, E. M. and Pennypacker, C. R.: Scattering and absorption of light by nonspherical dielectric grains, The Astrophysical Journal, 186, 705–714, 1973.

Sun, W., Fu, Q., and Chen, Z.: Finite-difference time-domain solution of light scattering by dielectric particles with perfectly matched layer absorbing boundary conditions, Appl. Optics, 38, 3141–3151, 1999.

Sun, W., Loeb, N., and Yang, P.: On the retrieval of ice cloud particle shapes from POLDER measurements, J. Quant. Spectrosc. Ra., 101, 435–447, 2006.

Takano, Y. and Liou, K. N.: Solar radiative transfer in cirrus clouds. Part I. Single-scattering and optical properties of hexagonal ice crystals, J. Atmos. Sci., 46, 3–19, 1989.

Takano, Y. and Liou, K. N.: Transfer of polarized infrared radiation in optically anisotropic media: application to horizontally oriented ice crystals., J. Opt. Soc. Am. A, 10, 1243-1256, 1993.

Um, J. and McFarquhar, G. M.: Single-scattering properties of aggregates of bullet rosettes in cirrus, J. Appl. Meteorol. Clim., 46, 757–775, doi:10.1175/JAM2501.1, 2007.

Um, J. and McFarquhar, G. M.: Single-scattering properties of aggregates of plates, Q. J. Roy. Meteor. Soc, 135, 291–304, doi:10.1002/qj.378, 2009.

Um, J. and McFarquhar, G. M.: Dependence of the single-scattering properties of small ice crystals on idealized shape models, Atmos. Chem. Phys., 11, 3159–3171, doi:10.5194/acp-11-3159-2011, 2011.

van Diedenhoven, B., Cairns, B., Geogdzhayev, I. V., Fridlind, A. M., Ackerman, A. S., Yang, P., and Baum, B. A.: Remote sensing of ice crystal asymmetry parameter using multi-directional polarization measurements – Part 1: Methodology and evaluation with simulated measurements, Atmos. Meas. Tech., 5, 2361–2374, doi:10.5194/amt-5-2361-2012, 2012.

van Diedenhoven, B., Cairns, B., Fridlind, A. M., Ackerman, A. S., and Garrett, T. J.: Remote sensing of ice crystal asymmetry parameter using multi-directional polarization measurements – Part 2: Application to the Research Scanning Polarimeter, Atmos. Chem. Phys., 13, 3185–3203, doi:10.5194/acp-13-3185-2013, 2013.

Van Diedenhoven, B., Fridlind, A. M., Cairns, B., and Ackerman, A. S.: Variation of ice crystal size, shape and asymmetry parameter in tops of tropical deep convective clouds, J. Geophys. Res.-Atmos., 119, 11809–11825, 2014.

Warren, S. G. and Brandt, R. E.: Optical constants of ice from the ultraviolet to the microwave: A revised compilation, J. Geophys. Res., 113, D14220, doi:10.1029/2007JD009744, 2008.

Yang, P. and Liou, K. N.: Geometric-optics-integral-equation method for light scattering by nonspherical ice crystals, Appl. Optics, 35, 6568–6584, 1996.

Yang, P. and Liou, K. N.: An efficient algorithm for truncating spatial domain in modeling light scattering by finite-difference technique, J. Comput. Phys., 140, 346–369, 1998a.

Yang, P. and Liou, K. N.: Single-scattering properties of complex ice crystals in terrestrial atmosphere, Contrib. Atmos. Phys., 71, 223–248, 1998b.

Yang, P., Liou, K. N., Wyser, K., and Mitchell, D.: Parameterization of the scattering and absorption properties of individual ice crystals, J. Geophys. Res., 105, 4699–4718, 2000.

Yang, P., Wei, H., Huang, H.-L., Baum, B. A., Hu, Y. X., Kattawar, G. W., Mishchenko, M. I., and Fu, Q.: Scattering and absorption property database for nonspherical ice particles in the near- through far-infrared spectral region, Appl. Optics, 44, 5512–5523, 2005.

Yang, P., Bi, L., Baum, B. A., Liou, K. N., Kattawar, G. W., Mishchenko, M. I., and Cole, B.: Spectrally consistent scattering, absorption, and polarization properties of atmospheric ice crystals at wavelengths from 02 to 100 µm, J. Atmos. Sci., 70, 330–347, 2013.

Yang, P., Liou, K. N., Bi, L., Liu, C., Yi, B. Q., and Baum, B. A.: On the radiative properties of ice clouds: Light scattering, remote sensing, and radiation parameterization, Adv. Atmos. Sci., 32, 32–63, 2015.

Yee, S. K.: Numerical solution of initial boundary value problems involving Maxwell's equations in isotropic media, IEEE Trans. Antennas Propag., 14, 302–307, 1966.

Yurkin, M. A., Maltsev, V. P., and Hoekstra, A. G.: The discrete dipole approximation for simulation of light scattering by particles much larger than the wavelength, J. Quant. Spectrosc. Ra., 106, 546–557, 2007.

Zhang, Z., Yang, P., Kattawar, G., Riedi, J., C.-Labonnote, L., Baum, B. A., Platnick, S., and Huang, H.-L.: Influence of ice particle model on satellite ice cloud retrieval: lessons learned from MODIS and POLDER cloud product comparison, Atmos. Chem. Phys., 9, 7115–7129, doi:10.5194/acp-9-7115-2009, 2009.